

Structure estimation of 2D listric faults using quadratic Bezier curve for depth varying density distributions

Roy Arka¹, Kumar Thatikonda Suresh¹, and Sharma Rajat Kumar¹

¹National Centre for Earth Science Studies

November 16, 2022

Abstract

A contemporary and decisive optimization algorithm is developed for inverting gravity anomalies due to listric faults. The cross-section of listric faults are generally concave up, and the dip of the fault plane gradually decreases with depth. Quadratic Bezier curves are utilized to represent the curvature of the fault plane. The densities of sediment deposition are assumed to be known and can take any functional form of depth. By constraining the density, a global optimization algorithm is adopted to estimate the fault structure by inverting control point parameters of Bezier curves. The presented algorithm is implemented in two different synthetic models having fixed and depth varying density contrasts. The robustness of the algorithm is authenticated by incorporating white Gaussian noise into synthetic gravity anomalies. A detailed uncertainty appraisal is also performed to justify the reliability of the algorithm. Finally, a real structure is reconstructed using observed gravity anomalies, and the estimated structure is verified with the structure obtained in previously published literature. Furthermore, a Matlab based GUI is developed such that any user can estimate real listric fault structure without any computational difficulties.

1 Structure estimation of 2D listric faults using quadratic Bezier
2 curve for depth varying density distributions

3 Arka Roy^{1,2}, Thatikonda Suresh Kumar¹, Rajat Kumar Sharma,¹

4 ¹National Centre for Earth Science Studies, Akkulam, Trivandrum, Kerala, India - 695011.

5 ²Cochin University of Science and Technology, Kochi, Kerala, India - 682022.

6 Key Points:

- 7
- 8 • Listric fault inversion from observed gravity anomalies
 - 9 • Fault plane parametrization using Bezier curve and optimization using PSO
 - Graphical User interface for inverting real fault structures

Corresponding author: Arka Roy, arka.phy@gmail.com

Abstract

A contemporary and decisive optimization algorithm is developed for inverting gravity anomalies due to listric faults. The cross-section of listric faults are generally concave up, and the dip of the fault plane gradually decreases with depth. Quadratic Bezier curves are utilized to represent the curvature of the fault plane. The densities of sediment deposition are assumed to be known and can take any functional form of depth. By constraining the density, a global optimization algorithm is adopted to estimate the fault structure by inverting control point parameters of Bezier curves. The presented algorithm is implemented in two different synthetic models having fixed and depth varying density contrasts. The robustness of the algorithm is authenticated by incorporating white Gaussian noise into synthetic gravity anomalies. A detailed uncertainty appraisal is also performed to justify the reliability of the algorithm. Finally, a real structure is reconstructed using observed gravity anomalies, and the estimated structure is verified with the structure obtained in previously published literature. Furthermore, a Matlab based GUI is developed such that any user can estimate real listric fault structure without any computational difficulties.

1 Introduction

Listric faults were first introduced by Suess (1909) for describing faults in coal mines in northern France. The fault planes of listric faults are generally upward concave in nature, and the dip decreases with depth (Shelton, 1984). Listric faults have particular importance in the formation of sedimentary basins. Most of the listric faults are generally occurs during the formation of rift or formation of passive continental margins (Bally et al., 1981). The curvature occurred due to the thick sediment depositions in case of boundary faults (Chakravarthi, 2011). Listric fault can produce structural trap by relative displacement of strata to create a barrier to petroleum migration (Sheth, 1998; Yamada & McClay, 2003). It also has structural importance for mineral explorations (Song et al., 2012). The gravity method is one of the oldest geophysical approaches for subsurface imaging. In general, gravity inversion for subsurface parameter estimation is non-unique but by incorporating proper constraints (Y. Li & Oldenburg, 1996; Portniaguine & Zhdanov, 2002) a stable and converging parameter optimization can be achieved. In our present study, the density contrast is assumed to be known from borehole logging and used as a constraint for fault structure estimation. Furthermore, an uncertainty appraisal provides a reliable solution for any ill-posed problem.

The gravity method is one of the passive geophysical techniques to study the interior of the Earth. The ground gravity survey is very fast, inexpensive, and can cover a large study area via non-destructive measurements. The gravity method plays a vital role in geological structure estimation and exploration purposes. There are numerous implementations, such as, structure estimation of sedimentary basins (Silva et al., 2006; Zhou, 2013; Pallero et al., 2015; A. Roy et al., 2021b), faults and folds (L. Roy et al., 2000; Chakravarthi & Sundararajan, 2004, 2007b; A. Roy & Kumar, 2021) due to crustal deformations, glaciology (Crossley & Clarke, 1970; Tinto & Bell, 2011) and hydro-geology (Alatorre-Zamora & Campos-Enriquez, 1991; Güntner et al., 2007) etc. The exploration study includes mining (Jaffal et al., 2010; Veiga & Gunson, 2020), hydrocarbon exploration (Rose et al., 2006; W. Li et al., 2016), cavity detection etc. The gravitational inversion is a useful tool to interpret the gravity data for subsurface imaging. Density and corresponding geometries of the subsurface structure are the two parameters for geophysical optimization using gravity anomalies. Optimization algorithms are referred to a mathematical procedure for finding parameters by minimizing the objective function. As per the algorithms' demand, one can categorize optimization algorithms as (1) algorithms that use derivative information, (2) algorithms that do not require derivative information of objective function. Here are a few examples of optimization algorithms that require derivative information for gravity inversion. Chakravarthi and Sundararajan (2007a, 2007b) used Marquardt optimization for structure estimation using gravity anomalies, Silva et al. (2014) developed a fast inversion

62 technique using Gauss-Newton optimization for inverting basement relief. Florio (2020) used
 63 iterative rescaling approach for evaluating 3D basement depth. Qin et al. (2016) inverted
 64 3D gravity anomalies using a non-linear conjugate gradient optimization algorithm. X. Feng
 65 et al. (2018) derived a combined multinorm and normalized vertical derivative technique for
 66 3D gravity inversion of basement relief. Most of the global optimization algorithm does not
 67 require any derivative information as well as any pre-requisite models. Such algorithms are
 68 mainly population-based and use iterative schemes for optimization. Some of the exam-
 69 ples of population-based algorithms that used in gravity inversion are differential evolution
 70 (Ekinici et al., 2016; A. Roy et al., 2021a), genetic algorithm (Zhang et al., 2004; Mon-
 71 tesinos et al., 2005), very fast simulated annealing (Nagihara & Hall, 2001; Biswas, 2015),
 72 ant colony optimization (Srivastava et al., 2014), particle swarm optimization (Pallero et
 73 al., 2015; Essa & Munsch, 2019) etc. Particle swarm optimization is one of the most pop-
 74 ular global optimization schemes due to its simple architecture, easy implementation and
 75 computational efficiency. Here we adapted PSO for optimizing listric fault structures from
 76 observed gravity anomalies.

77 Several authors performed an extensive study for inverting planner faults by different
 78 optimization techniques. Due to the fault structure’s geological importance, a continuous
 79 improvement of optimization algorithms is carried out for an accurate and fast converging
 80 structure estimation. In this direction Chakravarthi and Sundararajan (2004) derived an an-
 81 alytic ridge regression optimization technique for inclined fault inversion. Abdelrahman and
 82 Essa (2015) developed a least-square optimization, Essa (2013) performed a variance analy-
 83 sis method, Touthmalani (2013); Elhussain (2021) adopted PSO for dipping fault structure
 84 estimation having constant densities. In general, density can vary with depth for differ-
 85 ent types of sediment depositions, and incorporating variable density contrasts into models
 86 can provide accurate estimations. Minimal studies have been performed for inverting the
 87 listric fault plane from observed gravity anomalies. An automatic 2.5D listric fault inversion
 88 technique was developed by (Chakravarthi, 2011) for prescribed depth varying density con-
 89 trasts. Further (Chakravarthi, 2010; Chakravarthi et al., 2017) characterized the fault plane
 90 in terms of higher-order polynomials for depth varying density distributions. In our present
 91 study, the listric fault planes are expressed using a quadratic Bezier curve for inverting
 92 gravity anomalies and estimating the underneath fault structure. The new algorithm can
 93 invert the listric fault plane for any depth varying density distributions without any prior
 94 initial model requirements. It is the first time developing such an algorithm for optimizing
 95 the listric fault plane using a quadratic Bezier curve with fewer parameter requirements.

96 2 Materials and Methods

97 This section illustrates the mathematical formulation for evaluating gravity anomalies
 98 due to any irregular inhomogeneous 2D structures. The Newtonian potential is the founda-
 99 tion for any potential theories, and we consider it for estimating gravity anomalies due
 100 to underneath anomalous densities. Various analytical simplifications and numerical tech-
 101 niques were developed for the faster and accurate computations of the potential field for
 102 irregular geometries. Finally, we implement it for forward modelling of listric faults having
 103 depth varying density distribution.

104 2.1 Forward Modelling

105 Forward modelling is the nitty-gritty for any global optimization problem. A forward
 106 model needs to be evaluated repeatedly during the inversion process for parameter esti-
 107 mation. Hence an inexpensive and less complex but meticulous forward model is always
 108 desirable for any faster converging optimization problem. In figure 1, a 2D irregular geom-
 109 etry having anomalous density is shown, for which the gravity anomaly has to be obtained
 110 at any observation point P (x_i, z_i) . A convex polygon can approximate any irregular 2D
 111 shape (Talwani et al., 1959; Zhou, 2008, 2009; Wan & Zhang, 2019), and by increasing

112 the vertices of the polygon, it can more accurately mimic the original shape. Further, the
 113 vertical component of gravity anomaly (g_z) due to this strike infinite (y directional infinite
 114 extension) approximated 2D polygonal shape having density contrast $\Delta\rho$ can be estimated
 115 as a surface integral (Talwani et al., 1959) form

$$g_z(x_i, z_i) = 2G \iint_S \frac{\Delta\rho \cdot (z - z_i)}{(x - x_i)^2 + (z - z_i)^2} dx dz, \quad (1)$$

116 Where G is the universal gravitational constant. The density can vary anomalously
 117 in the horizontal and vertical directions. However, in our present study, we consider only
 118 depth varying density distribution $\Delta\rho(z)$, having any functional form of z . Using Stokes'
 119 theorem, the 2D area integral of irregular shape having depth varying density contrast can
 120 be converted into a line integral as

$$g_z(x_i, z_i) = -2G \oint \Delta\rho \cdot \arctan\left(\frac{x - x_i}{z - z_i}\right) dz \quad (2)$$

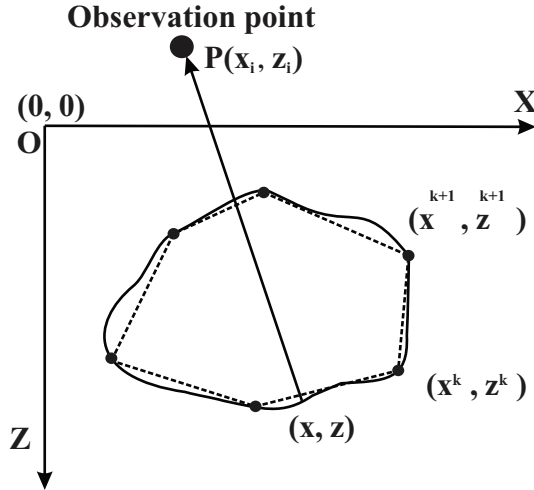


Figure 1. Polygon approximation of 2D irregular structure. The solid line represents the real mass source, and the dotted line represents approximated model.

121 The line integral can be numerically evaluated using Gauss Legendre quadrature for-
 122 mulation (Winckel, 2004). Let us assume the 2D irregular structure is approximated using
 123 a polygon (Figure 1) having N vertices, where (x^k, z^k) and (x^{k+1}, z^{k+1}) are two consecutive
 124 vertices. Hence the vertical component of gravity anomaly at any surface point $P(x_i, z_i)$
 125 due to the anomalous contrast $\Delta\rho(z)$ is expressed as

$$g_z(x_i, z_i) = -2G \sum_{k=1}^{N-1} \int_{z_k}^{z_{k+1}} \Delta\rho(z) \cdot \arctan\left(\frac{x - x_i}{z - z_i}\right) dz \quad (3)$$

126 In our present study, the prime objective is to invert gravity anomalies for inverting
 127 listric fault structure, and forward modelling of listric fault is an essential step for optimiza-
 128 tion. In figure 2, a generic architecture of the listric fault is shown, and the structure can
 129 be expressed by a polygon having four vertex points. In table 1, the locations of vertex

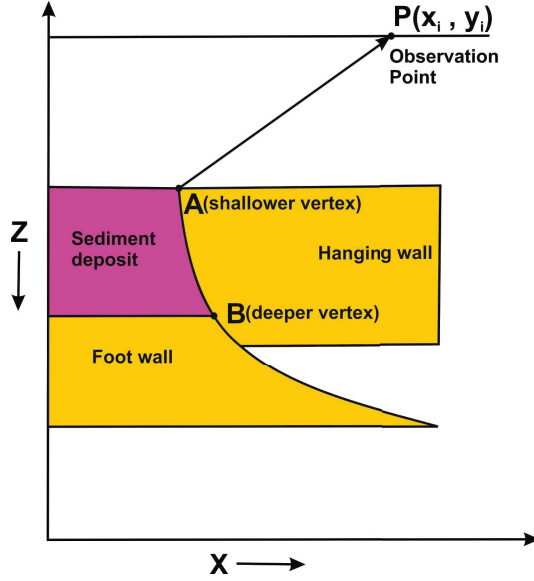


Figure 2. Generic representation of listric fault structure. AB represents the fault plane, and P is the observation point for estimating gravity anomalies.

130 points are given as per the orientation of the fault plane. Finally, the curvature of the listric
 131 fault plane is obtained using the quadratic Bezier curve. Hence, with the help of those four
 132 vertex points and locations of the fault plane from the Bezier curve, the forward model of
 133 any listric fault can be approximated. The vertical component of gravity anomaly can be
 134 estimated from the numerical line integral formulation using Gauss Legendre quadrature.

Table 1. Vertex locations for any generalized listric fault plane.

Vertex count	Left side oriented	Right side oriented
1 st (Point A)	(x_s, z_s)	(x_s, z_s)
2 nd (Point B)	(x_d, z_d)	(x_d, z_d)
3 rd	$(-\infty, z_d)$	(∞, z_d)
4 th	$(-\infty, z_s)$	(∞, z_s)

135 **2.2 Inverse Modelling**

136 Inverse modelling in geophysics is an optimization process for estimating geophysical
 137 parameters of underneath geological structures by minimizing misfit error between observed
 138 and estimated field data. Various optimization algorithms can invert such geophysical data
 139 in a more or less intelligent and efficient way. In general, geophysical inverse problems
 140 are non-unique, i.e. minimum misfit error can be found for different sets of optimizing
 141 parameters. In other words, different geological structures can provide the same observed
 142 field data. By incorporating any prior information about the parameters can reduce such
 143 non-uniqueness. The apriori pieces of information are fused into optimization algorithms as
 144 a constraint to invert the observed data for getting unique structures.

145 In our present study, the aim is to optimize listric fault structure by inverting observed
 146 gravity anomalies. The curvature of the listric fault plane can be expressed using quadratic
 147 Bezier curves. The weights of control points are the only parameters to represent the
 148 curved fault plane. There are six control points required to parametrize a 2D listric fault
 149 plane, and the corresponding weights are used as a model parameter in our optimization
 150 problems. By further constraining one control point, five model parameters are sufficient to
 151 invert the observed gravity anomalies to optimize any listric fault structure. The details of
 152 implementing constraints are discussed in the preceding section.

153 Optimization algorithms are the main building blocks for an inverse problem. Nowa-
 154 days, swarm-based algorithms are popular in various science and engineering disciplines
 155 due to their robustness and flexibility. These are mainly global optimization algorithms in-
 156 spired by the mass behaviour of social animals, suitable for a multi-dimensional real-valued
 157 optimization problem. PSO is one of the most potent meta-heuristic numerical global op-
 158 timization algorithms applied in many fields due to its flexibility and simplicity. PSO was
 159 first introduced by Eberhart and Kennedy (1995), and it is inspired by the cumulative social
 160 behaviour of animals like a school of fishes or flock of birds. Our present study uses PSO
 161 as an optimization algorithm for inverting observed gravity anomalies for estimating listric
 162 fault structures. PSO is straightforward to implement, and it is independent of initial pa-
 163 rameter selection. A detailed scheme (Marini & Walczak, 2015) of the basic PSO algorithm
 164 is shown in figure 3.

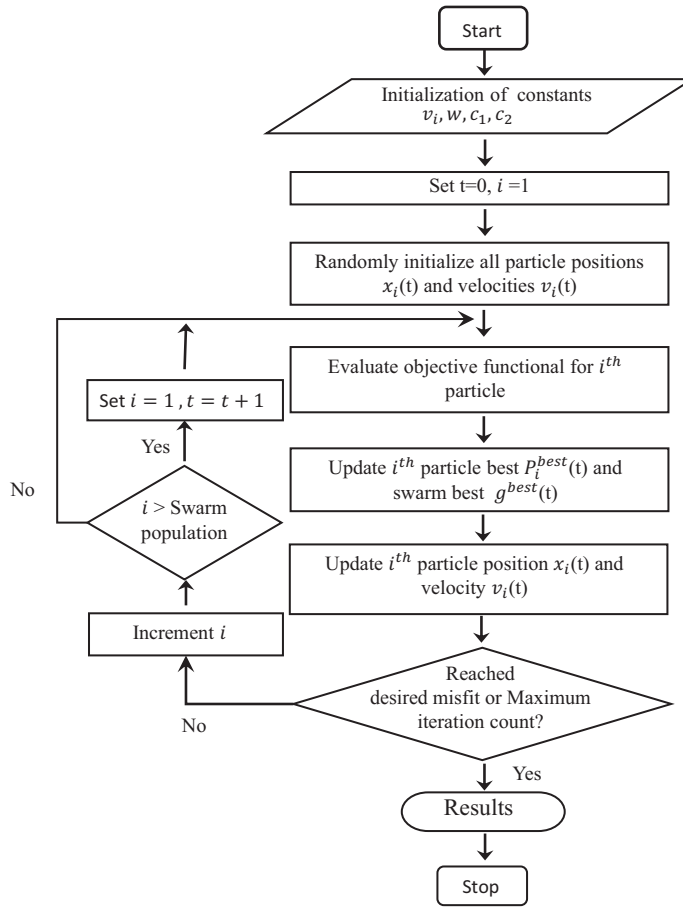


Figure 3. Scheme of the basic PSO algorithm.

165 Let us assume $f_z(x_j, z_j)$ is the observed gravity anomaly and $g_z(x_j, z_j)$ is the predicted
 166 gravity anomaly at any observed point (x_j, z_j) due to some model parameter X_i . Then the
 167 objective function can be written as

$$Q = \sum_{i=1}^k (f_z(x_j, z_j) - g_z(x_j, z_j))^2. \quad (4)$$

168 Where k is the number of observation points, let us assume S is a D -dimensional search
 169 space for optimizing the objective function. In PSO, each candidate solution is known as
 170 ‘particle’, and each particle consists of D number of parameters that have to be optimized.
 171 At any time step t , the i^{th} particle can be represented as a vector $X_i(t)$ in the search space
 172 as

$$X_i(t) = [x_{i1}, x_{i2}, x_{i3}, \dots, x_{iD}], \text{ where } i \in \{1, 2, 3, \dots, N\} \quad (5)$$

173 and the swarm consist of N particles having dimension D . During the optimization
 174 process, the position of each particle updates for two consecutive time steps and follows the
 175 relation

$$X_i(t+1) = X_i(t) + V_i(t+1). \quad (6)$$

176 Where $V_i(t+1)$ is the velocity component of i^{th} particle at time step $t+1$. The velocity
 177 component also updates as follow

$$V_i(t+1) = wV_i(t) + c_1r_1(P_i^{\text{best}}(t) - V_i(t)) + c_2r_2(g^{\text{best}}(t) - V_i(t)). \quad (7)$$

178 Where c_1, c_2 are real valued constant term named acceleration coefficients and r_1, r_2
 179 are uniformly distributed random numbers having range $[0,1]$. $P_i^{\text{best}}(t)$ is the parameters
 180 of best solution ever obtained by i^{th} particle termed as personal best and $g^{\text{best}}(t)$ is the
 181 parameters of best solution obtained by entire swarm as known as global best. The term
 182 $wV_i(t)$ is named inertia term and $c_1r_1(P_i^{\text{best}}(t) - V_i(t))$, $c_2r_2(g^{\text{best}}(t) - V_i(t))$ are termed as
 183 cognitive component and social component respectively. Usually the range for c_1, c_2 varies
 184 from $[0 < c_1, c_2 < 2]$ during the selection and a detailed parameter tuning is required for
 185 faster convergence of model parameters. A criterion for stable convergence developed by
 186 Perez and Behdinan (2007) are as follows

$$0 < c_1 + c_2 < 4, \quad (8)$$

$$\left(\frac{c_1 + c_2}{2} - 1 \right) < w < 1. \quad (9)$$

187 The inertia coefficient (w) plays an important role to bypass uncontrolled velocity that
 188 can cause the divergence of the optimization problem. A perfect balance between explo-
 189 ration and exploitation is much needed for any global optimization problem. By tuning the
 190 inertia term, velocity modulation can be controlled. For larger inertia weight, it facilitates
 191 global search that covers the entire search space, where smaller inertia weight assists local
 192 exploitation. A higher value of inertia weight is always desirable during initial iterations,

193 followed by smaller inertia weight at maximum iterations. An effective arrangement for the
 194 steady reduction of inertia weight is desirable for optimization. In this direction Shi and
 195 Eberhart (1998) used random inertia weight, Arumugam and Rao (2006) used global-local
 196 best inertial weight, Y. Feng et al. (2007) developed chaotic descendent inertia weight, etc.
 197 In our present study, a linearly decreasing inertia weight proposed by Xin et al. (2009) is
 198 used for the optimization problem. The dynamic adjustment strategies become

$$w_t = w_{max} - \left(\frac{w_{max} - w_{min}}{t_{max}} \right) \times t, \quad (10)$$

199 where $w(t)$ is the inertia weight at t^{th} time step. w_{max} and w_{min} are the maximum and
 200 minimum range of w that can be obtained from acceleration coefficients shown in equation
 201 9. t_{max} is the maximum time step for the optimization algorithm.

202 2.3 Bezier curves and cost function

203 Bezier curve was first introduced by French engineer Pierre Bezier for designing the
 204 bodywork of automobiles. Bezier curves have many applications in science, engineering
 205 designing, computer-aided design systems, animation, robotics, networks, etc. The main
 206 advantage of Bezier curves is that they are computationally simple and stable. The math-
 207 ematical descriptions are compact, intuitive and elegant. It is easy to compute and able to
 208 represent any shape of a curve. The mathematical basis for Bezier curves is the Bernstein
 209 polynomials. The basis vectors are summed up with the help of some set of control points
 210 to represent any curve. The Bezier curve can be expressed mathematically as

$$z(t) = \sum_{i=0}^n P_i B_i^n(t), \quad (11)$$

where P_i are the set of control points and $B_i^n(t)$ are the Bernstein polynomials. The
 Bernstein polynomials are represented as

$$B_i^n(t) = \binom{n}{i} (1-t)^{n-i} t^i, \text{ for } 0 < t < 1. \quad (12)$$

211 Where n is the degree of the polynomial. For any quadratic Bezier curve, three control
 212 points are required, and the path traced by the function $Z(t)$ can be written as

$$Z(t) = (1-t)[(1-t)P_0 + tP_1] + t[(1-t)P_1 + tP_2], \text{ for } 0 < t < 1. \quad (13)$$

213 In our present study, the listric fault plane can be represented by a quadratic Bezier
 214 curve for lessening the parameters for optimization. The listric fault lies in a 2D plane;
 215 hence, each control point's dimension is also two for representing the fault plane. That
 216 implies, in total, six parameters are required to be optimized. The first and last control
 217 points are always the endpoints of the curve for any Bezier curves. As the shallower vertex
 218 of the fault is lying on the surface, we can be constraining the vertical position of the first
 219 point that can reduce one parameter. Hence the number of actual parameters is five to
 220 optimize the fault plane. The gravity anomaly due to the parametrized fault plane can be
 221 obtained from the line integral (equation 3). Let us assume the operator $\hat{\chi}$ can evaluate the
 222 gravity anomaly due to the fault plane parametrized by the Bezier curve. Hence the cost
 223 function for the optimization problem can be written as

$$\begin{aligned}
 Q &= \sum_{i=1}^n (f_z(x_j, z_j) - g_z(x_j, z_j))^2 \\
 &= \sum_{i=1}^n (f_z(x_j, z_j) - \hat{\chi}(Z(t_i)))^2 \\
 &= \sum_{i=1}^n (f_z(x_j, z_j) - \hat{\chi}(\sum_{j=0}^k P_j B_j^k(t_i)))^2.
 \end{aligned} \tag{14}$$

224 Hence the cost function only depends on control point parameters P_j of the quadratic
 225 Bezier curve. PSO is used here for optimizing the cost function, and the optimized pa-
 226 rameters are further used to reconstruct the listric fault plane. Few synthetic models, a
 227 detailed uncertainty appraisal and application of real listric fault is discussed in detail in
 228 the preceding section.

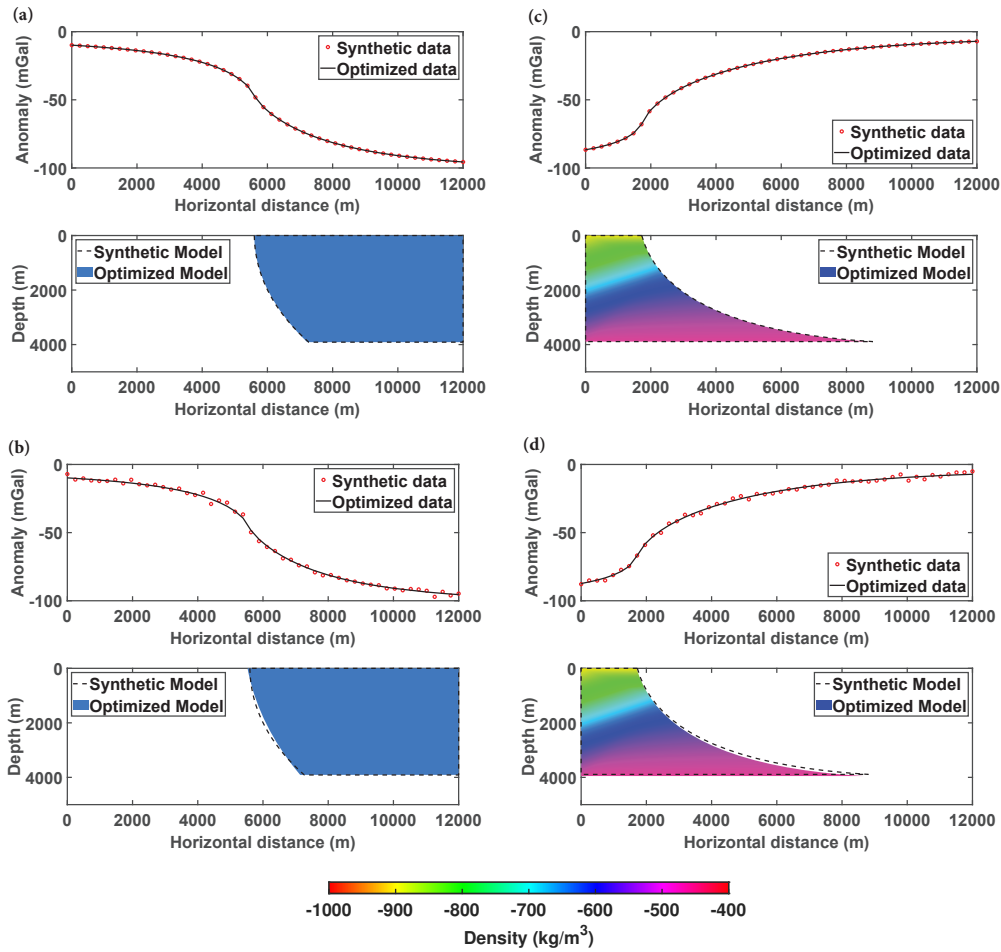


Figure 4. Inverted listric fault structure from synthetic gravity anomalies for (a) Model 1 without noise, (b) Model 1 with noise, (c) Model 2 without noise, and (d) Model 2 with noise. The synthetic gravity anomalies are denoted with the red dotted curve, and the optimized anomalies are shown in the upper panel denoted as the solid blue line. The inverted fault structures are represented as filled regions, and the actual structures are denoted by the black dashed line.

3 Results

In this section, the application of the developed algorithm is performed for various synthetic and real models. PSO is used here as an optimization algorithm, and all control parameters of PSO are tuned for faster convergence of model parameters. Two different types of density distributions, (1) uniform density contrast and (2) depth varying density contrast, are applied to evaluate the versatility of the algorithm. Further, all synthetic models are contaminated with white Gaussian noise to check the algorithm robustness.

3.1 Synthetic Models

Gravity anomalies for two different synthetic fault structures are inverted using the developed algorithms having predefined density distributions. A normal listric fault with fixed density distribution is defined as model 1, and model 2 consists of reverse listric fault with exponential density distributions shown in figure 4. The gravity anomalies for models 1 and 2 are further contaminated with Gaussian noise having a mean of 0 mGal and a standard deviation of 1.5 mGal. The profile length for gravity anomalies for both the models is around 12 km long with a maximum depth of 3.9 km for model 1 and 3.8 km for model 2. In total, 50 equidistant data points are considered for the inversion of gravity anomalies. We have considered a uniform density distribution for model 1, with a density contrast of -650 kg/m^3 and exponential depth varying density distribution for model 2. The density contrast for model 2 is

$$\Delta\rho(z) = (-0.40 - 0.5 \times \exp(-0.5 \times z \times 10^{-3})) \times 1000 \quad \text{kg/m}^3. \quad (15)$$

Our algorithm is versatile enough to invert any mathematical form of depth varying density distribution regardless of uniform and exponential density contrast.

Table 2. Comparison for both the models in terms of depth, Frechet distance and rms error of gravity anomaly.

Model type	Depth (m)	Frechet distance (m)	rms error (mGal)
Model 1 true	3912.10	-	-
Model 1 inverted noise free	3911.72	66.99	2.81×10^{-3}
Model 1 inverted with noise	3898.80	360.92	1.98×10^0
Model 2 true	3891.02	-	-
Model 2 inverted noise free	3891.41	69.51	9.57×10^{-3}
Model 2 inverted with noise	3890.65	550.60	3.03×10^0

In PSO algorithm, the control parameters are acceleration coefficients (c_1 , c_2), total population of the swarm (nPoP) and inertia weight(w). The inertia weights are dynamically adjustable and linearly varying as shown in equation 10. The swarm population plays a pivotal role in the convergence speed. By increasing the swarm population, convergence is achieved in lesser iterations by broadening the computational time. Hence a perfect balance between convergence speed and iteration counts are required for an inexpensive model. Similarly, the acceleration coefficients are also varying from a range [0, 2]. A detailed parameter tuning is required for faster converging and accurate parameter optimization. In this direction, both the models run for a nPoP range [0, 100], acceleration coefficient range of [0, 2] with a maximum time step of 1000 and relative misfit cut-off of an order of 10^{-3} . In

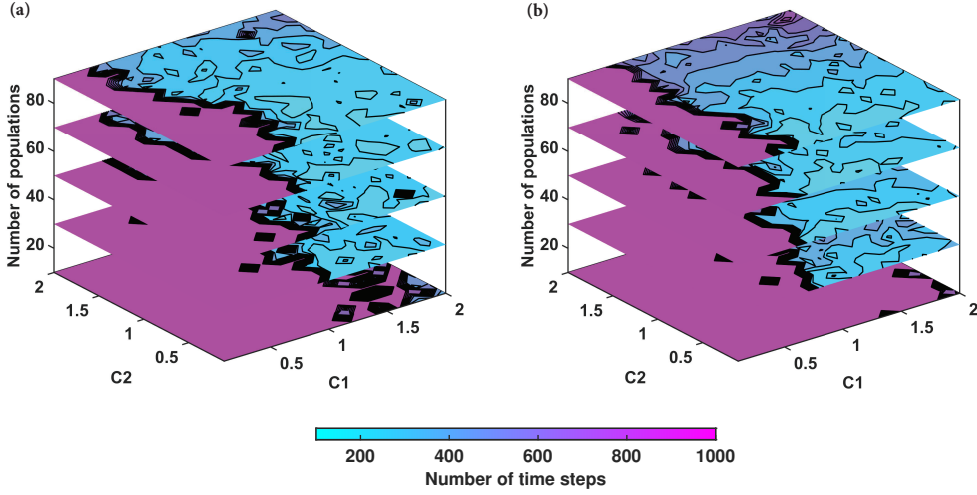


Figure 5. Parameter tuning for acceleration coefficients (c_1, c_2) and swarm population (nPoP) in terms of time steps for (a) Model-1 and (b) Model-2.

260 figure 5, a detailed stack plot for number of iteration count for various range of nPoP, c_1 and
 261 c_2 are shown. It can be observed that for nPoP greater 20, and acceleration coefficient range
 262 $1.4 < c_1 < 2.0$ and $0.2 < c_2 < 2.0$, both the models converge with minimum iteration count.
 263 The time range also varies for [10, 20] seconds by increasing the population count. Hence in
 264 our presented algorithm we choose the nPoP = 40, $c_1=1.4$ and $c_2=1.7$ as an optimal choice
 265 of control parameter for any synthetic and real data inversion.

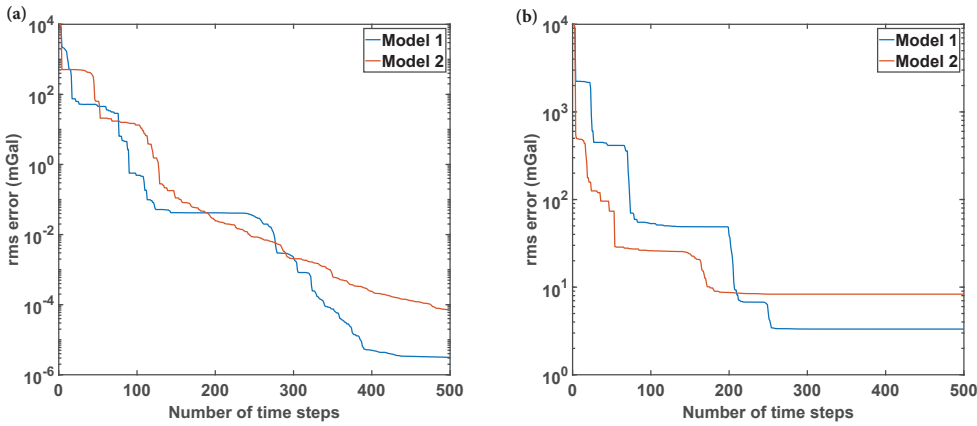


Figure 6. rms error plot of actual and inverted gravity anomalies with respect to time steps for (a) Model-1 and (b) Model-2.

266 After selecting the control parameters for PSO, the gravity anomalies for both the
 267 models are inverted and compare with the true structures of synthetic listric faults as shown
 268 in figure 4. Both the gravity anomalies are incorporated with noise, and the noisy data are
 269 inverted to check the robustness of the presented scheme. A detailed comparison for true
 270 model and inverted model for both noisy and noise-free data are shown in table 2. Here

271 we use Frechet distance to measure the deviation of fault planes from true models and
 272 inverted models. Frechet distances are utilized for the measuring of similarities between
 273 irregular curves. It is generally used to measure the similarities between trajectories of
 274 moving objects. Here we have used it as a performance parameter of our model to check the
 275 algorithm's accuracy. The higher value of Frechet distance indicating more dissimilarities
 276 of the model and vice versa. In the optimization process for each model, five independent
 277 model runs are performed for maximum time steps of 500. The minimum misfit error out
 278 of all independent runs is considered the best-inverted model, and the corresponding model
 279 parameters are used to reconstruct the fault plane. Finally, the rms error in each time step
 280 is plotted for noisy and noise-free models as shown in figure 6. It can be observed that
 281 the minimum misfit error for noise-free models are the order of 10^{-7} and for noisy data is
 282 10^{-2} for both the model configurations. The convergence achieves before the maximum time
 283 step. Unlike the inversion of any other potential field problem, gravity inversion is also non-
 284 unique, and data acquisition is erroneous due to noise incorporation. Here we incorporated
 285 density distribution as a constraint to get a unique, optimized structure. However, a proper
 286 uncertainty appraisal is a pivotal step to access the reliability of the inverted structures.
 287 Fernández-Martínez et al. (2013); Pallero et al. (2015) applied an equivalent region approach
 288 using cost function topography in a 2D PCA plane to evaluate the uncertainty analysis. We
 289 also adopted the same technique for the uncertainty appraisal for both models. The misfit
 290 error between observed and inverted anomalies gradually decreases during the optimisation
 291 process, and the optimizing parameters converge to the true solution. An equivalent region
 292 is a 2D space where all solutions below some predefined relative misfit cutoff are preserved.
 293 The relative misfit between observed and inverted gravity anomaly can be defined as

$$\phi_{rel} = \frac{\|f_z - g_z\|_2}{\|f_z\|_2} \times 100. \quad (16)$$

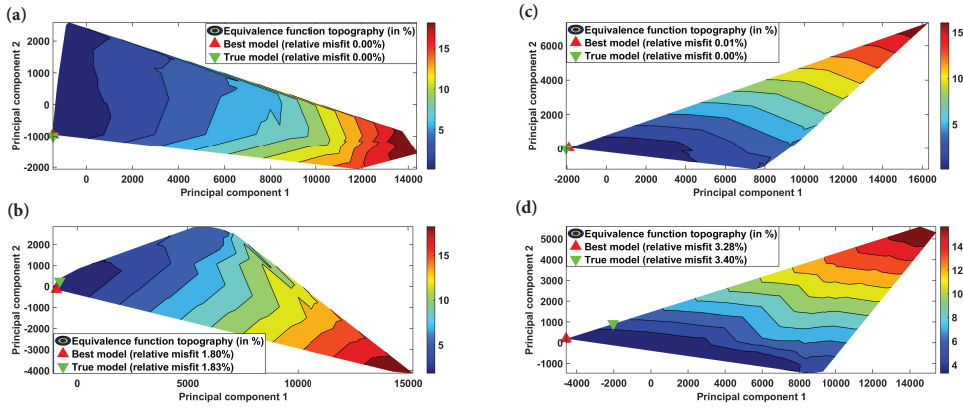


Figure 7. Equivalence function topography in 2D PCA plane for (a) Model 1 noise-free data, (b) Model 1 noise incorporated data, (c) Model 2 noise-free data, (d) Model 2 noise incorporated data.

294 In general, the cut off for relative misfit is 2-5 times the noise incorporation. Here for
 295 both the models, the minimum noise is around 5%, and the cutoff is considered as 25%. Let
 296 us assume $X = [S_1, S_2, \dots, S_q]$ are the solution set that satisfies the cutoff criterion. Each
 297 solution set consists of five parameters of Bezier curves control points that represent the
 298 listric fault plane. In the next step, a covariance matrix is constructed using the matrix
 299 formed by the solution set. Here X represents a matrix whose column vectors are the
 300 solution set, the covariance matrix having the form

$$C = (X - \mu)^T \cdot (X - \mu), \quad (17)$$

301 where μ is the mean of the solution set, the primary purpose of the covariance matrix is
 302 to find the eigenvectors and construct a PCA space to project all solutions and get a better
 303 visual representation. The first two eigenvectors corresponding to leading eigenvalues are
 304 known as principal components that form a 2D PCA space to represent the misfit error as
 305 a contour plot which is shown in figure 7 for both the models. All models are converged
 306 within a maximum iteration of 500. The parameters achieved in the last iteration of the
 307 algorithm are known as the best model, and the parameters for the actual synthetic model
 308 are known as the true model. When the gravity anomaly for all synthetic models are not
 309 contaminated with noise, the true model and best model coincides in the 2D PCA plane and
 310 located at the lowest misfit region. The true and best models are not coinciding for noisy
 311 data but are situated at the lowest misfit region. The relative misfit error for the true model
 312 is greater than the best-optimized model. These are the primary outcomes of uncertainty
 313 appraisal for the reliability of the inverted model.

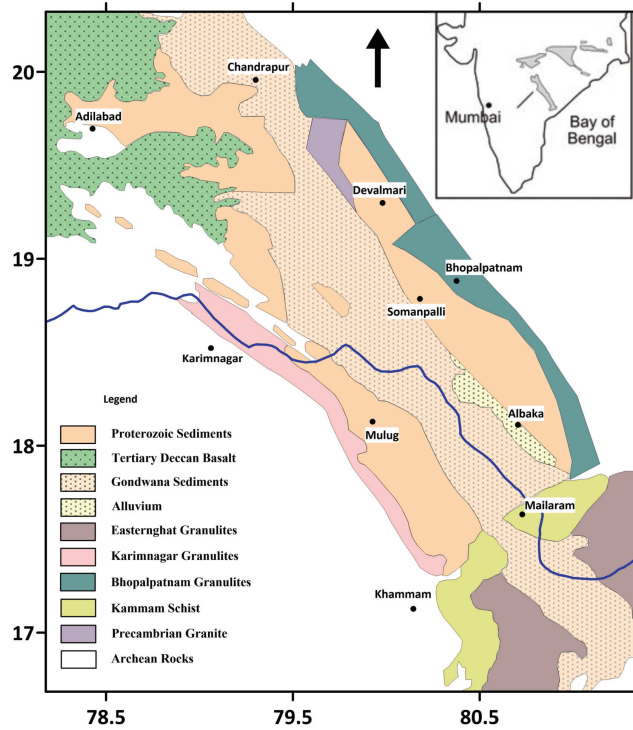


Figure 8. Geology map for Pranhita-Godavari valley obtained from Amarasinghe et al. (2014)

3.2 Real Model

314

315 In the previous section, different combinations of synthetic fault structures are in-
 316 verted, providing an accurate, robust, and reliable solution from observed gravity anom-
 317 alies. Here the optimization technique is applied to invert real gravity anomalies due to
 318 listric fault having depth varying density distribution from Godavari sub-basin. The se-
 319 quences of Gondwana are obtained in the southern part of the Indian subcontinent. The
 320 NW-SE trending Pranhita-Godavari valley is one of the major repositories of the Gond-
 321 wana successions. Pranhita-Godavari valley is further divided into four sub-basins such as
 322 Krishna-Godavari, Godavari, Chintalpudi and Kothagudem based on the nature of lithologic

323 sequences (Ramanamurthy & Parthasarathy, 1988). A detailed geology map is shown in
 324 figure 8. The northeastern side of the Godavari sub-basin is characterized by a half-graben
 325 structure named as Ahiri-Cherla master fault (Qureshy et al., 1968). Chakravarthi and
 326 Sundararajan (2004) inverted gravity anomalies to estimate a planner fault structure due
 327 to parabolic density distribution. Further Chakravarthi et al. (2017) inverted the observed
 328 gravity anomalies to estimate the listric fault plane using higher-order polynomials.

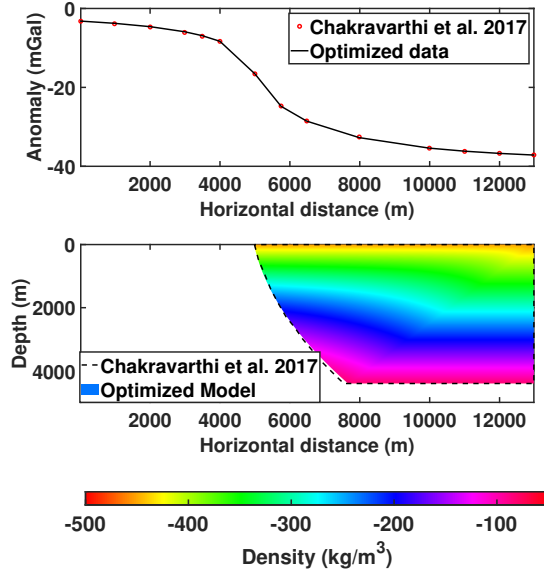


Figure 9. Inverted structure for Ahiri-Cherla master fault. The observed gravity anomalies are denoted with the red dotted curve, and the optimized anomalies are shown in the upper panel denoted as the solid blue line. The inverted fault structures are represented as filled regions, and the structure obtained by (Chakravarthi et al., 2017) are denoted by the black dashed line.

329 In our present study, the Bouguer anomaly throughout the Ahiri-Cherla master fault
 330 is inverted using the Bezier curve and compared the result obtained by Chakravarthi et al.
 331 (2017). The density contrast is obtained from borehole logging and fitted exponentially as
 332 follows

$$\Delta\rho(z) = (-0.4554 \times \exp(-0.3929 \times z \times 10^{-3})) \times 1000 \quad \text{kg/m}^3. \quad (18)$$

333 A rigorous gravity survey throughout the Godavari sub-basin was performed by Mishra
 334 et al. (1989). A 13 km long gravity anomaly profile was digitized from Chakravarthi and
 335 Sundararajan (2004); Chakravarthi et al. (2017) along the fault plane. The residual gravity
 336 anomaly is inverted using the presented algorithm, and the estimated structure is shown in
 337 figure 9. The Frechet distance between the inverted fault plane using the Bezier curve and
 338 using higher-order polynomial by Chakravarthi et al. (2017) are around 272.63 m. which
 339 indicates the good agreement with the structure estimation with the earlier work. The max-
 340 imum depth is about 4404.85 m, and the rms error between observed and estimated gravity
 341 anomalies is 0.3705 mGal. Hence, the Bezier curve optimized model is less parametrized
 342 and accurately estimates the listric fault plane for a real scenario.

4 Graphical User Interface

A compact and user-friendly Matlab based graphical user interface named ‘ListicFault-Inv’ is developed to estimate the underneath listric fault structure due to any depth varying density distribution from observed gravity anomalies. Any prerequisite knowledge of programming language or detailed understanding of the present algorithm is not needed to estimate fault structure from observed gravity anomalies. The GUI popped up by running the Matlab file ‘ListicFaultInv.m’, and it is auto adjustable as per the screen resolution shown in figure 10. Two ASCII text files containing the gravity anomaly and corresponding observation points are required for the optimization. Gravity anomalies must have to be in the mGal unit, and observation points are in meters. Two dedicated browser buttons are provided for importing the data. The functional form of depth varying density distribution are also required as model input parameters.

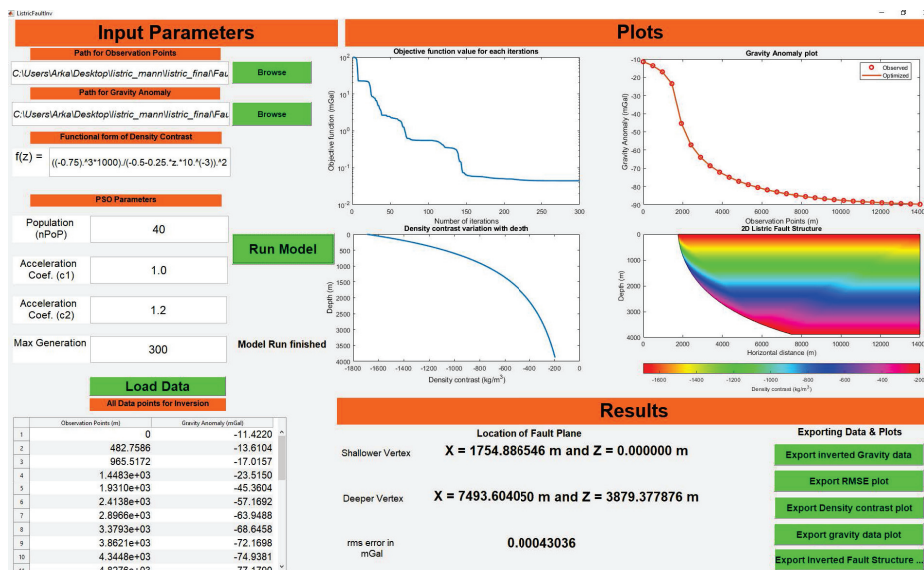


Figure 10. The user interface of ListicFaultInv GUI.

Although the control parameters of PSO algorithm are tuned initially, in this GUI, any user can change the control parameters as per their choice. Finally, a push-button named ‘load data’ is provided for showcasing the observed anomalies at different observation points in a separate tabular format. Only this information is needed to run the model for structural estimation. Finally, by clicking the ‘run model’ button, four plots are generated at the end of the optimization problem. The plots are listric fault structure, observed and inverted gravity anomaly, objective function value after each iteration and the depth varying density contrast plot. All optimized data and plots can be exported in any existing file format. The location of the shallower and the deeper vertex of the fault plane, the rms error of observed, and inverted gravity anomalies can be shown in the result section.

5 Conclusion

In this paper, our primary motivation is to provide some insight to develop a unified algorithm for inverting gravity anomalies due to any listric fault structures. A detailed uncertainty appraisal is performed in different synthetic models for the reliability of the algorithm. The versatility of the algorithm is that it can invert gravity anomalies due to any depth varying density distributions. Furthermore, no prior model selection is required due to the usage of global optimization. It is the first time representing the fault plane in terms

372 of the Bezier curve by adjusting the control points. It also required a fixed number of model
 373 parameters to reconstruct any complicated structures. Finally, a graphical user interface is
 374 designed to visualize any fault structure reconstruction without any computational difficul-
 375 ties. The presented algorithm is demonstrated for real fault structure estimation from the
 376 Godavari sub-basin, and the obtained structure provides good agreement with previously
 377 published literature.

378 6 Data Availability Statement

379 All computational codes and synthetic data can be obtained from Github public repos-
 380 itory link <https://github.com/ArkaRoy-Matlab/ListricFault> . The observed gravity
 381 anomaly data for real listric fault structure is digitized from the paper [Chakravarthi, V.,
 382 Kumar, M. P., Ramamma, B., & Sastry, S. R. (2017). Gravity anomaly interpretation of
 383 2D fault morphologies by means of nonplanar fault planes and exponential density contrast
 384 model: a space domain technique. *Arabian Journal of Geosciences*, 10(3), 64].

385 Acknowledgments

386 We thank the Director, NCESS, and the Secretary, MoES, Government of India, for pro-
 387 viding funds and unconditional support to carry out this work. We are also thankful to
 388 the former Director of NCESS, P. C. Rao, and the deputy group head, J. K. Tomsom, who
 389 imparted thoughtful suggestions. We thank Nilanjana Sorcar for her helpful discussions.

390 References

- 391 Abdelrahman, E., & Essa, K. (2015). Three least-squares minimization approaches to
 392 interpret gravity data due to dipping faults. *Pure and Applied Geophysics*, 172(2),
 393 427–438.
- 394 Alatorre-Zamora, M.-A., & Campos-Enriquez, J.-O. (1991). La primavera caldera (mexico):
 395 structure inferred from gravity and hydrogeological considerations. *Geophysics*, 56(7),
 396 992–1002.
- 397 Amarasinghe, U., Chaudhuri, A., Collins, A., Deb, G., & Patranabis-Deb, S. (2014, 04).
 398 Evolving provenance in the proterozoic pranhita-godavari basin, india. *Geoscience*
 399 *Frontiers*, 6. doi: 10.1016/j.gsf.2014.03.009
- 400 Arumugam, M. S., & Rao, M. (2006). On the performance of the particle swarm optimization
 401 algorithm with various inertia weight variants for computing optimal control of a class
 402 of hybrid systems. *Discrete Dynamics in Nature and Society*, 2006.
- 403 Bally, A., Bernoulli, D., Davies, G., & Montadert, L. (1981). Listric normal faults.
 404 *Oceanologica Acta*, Special issue.
- 405 Biswas, A. (2015). Interpretation of residual gravity anomaly caused by simple shaped
 406 bodies using very fast simulated annealing global optimization. *Geoscience Frontiers*,
 407 6(6), 875–893.
- 408 Chakravarthi, V. (2010). Gravity anomalies of 2d fault structures with fault planes described
 409 by polynomial functions of arbitrary degree. *Current Science* (00113891), 99(5).
- 410 Chakravarthi, V. (2011). Automatic gravity optimization of 2.5 d strike listric fault sources
 411 with analytically defined fault planes and depth-dependent density. *Geophysics*, 76(2),
 412 I21–I31.
- 413 Chakravarthi, V., Kumar, M. P., Ramamma, B., & Sastry, S. R. (2017). Gravity anomaly
 414 interpretation of 2d fault morphologies by means of nonplanar fault planes and ex-
 415ponential density contrast model: a space domain technique. *Arabian Journal of*
 416 *Geosciences*, 10(3), 64.
- 417 Chakravarthi, V., & Sundararajan, N. (2004). Ridge-regression algorithm for gravity inver-
 418sion of fault structures with variable density. *Geophysics*, 69(6), 1394–1404.
- 419 Chakravarthi, V., & Sundararajan, N. (2007a). 3d gravity inversion of basement relief—a
 420 depth-dependent density approach. *Geophysics*, 72(2), I23–I32.

- 421 Chakravarthi, V., & Sundararajan, N. (2007b). Marquardt optimization of gravity anomalies
422 of anticlinal and synclinal structures with prescribed depth-dependent density.
423 *Geophysical prospecting*, 55(4), 571–587.
- 424 Crossley, D. J., & Clarke, G. K. (1970). Gravity measurements on “fox glacier”, yukon
425 territory, canada. *Journal of Glaciology*, 9(57), 363–374.
- 426 Eberhart, R., & Kennedy, J. (1995). A new optimizer using particle swarm theory. In
427 Mhs’95. proceedings of the sixth international symposium on micro machine and hu-
428 man science (pp. 39–43).
- 429 Ekinci, Y. L., Balkaya, Ç., Göktürkler, G., & Turan, S. (2016). Model parameter estima-
430 tions from residual gravity anomalies due to simple-shaped sources using differential
431 evolution algorithm. *Journal of Applied Geophysics*, 129, 133–147.
- 432 Elhussein, M. (2021). New inversion approach for interpreting gravity data caused by
433 dipping faults. *Earth and Space Science*, 8(2), e2020EA001075.
- 434 Essa, K. S. (2013). Gravity interpretation of dipping faults using the variance analysis
435 method. *Journal of Geophysics and Engineering*, 10(1), 015003.
- 436 Essa, K. S., & Munsch, M. (2019). Gravity data interpretation using the particle swarm
437 optimisation method with application to mineral exploration. *Journal of Earth System
438 Science*, 128(5), 1–16.
- 439 Feng, X., Wang, W., & Yuan, B. (2018). 3d gravity inversion of basement relief for a rift
440 basin based on combined multinorm and normalized vertical derivative of the total
441 horizontal derivative techniques. *Geophysics*, 83(5), G107–G118.
- 442 Feng, Y., Teng, G.-F., Wang, A.-X., & Yao, Y.-M. (2007). Chaotic inertia weight in particle
443 swarm optimization. In *Second international conference on innovative computing,
444 informatio and control (icicic 2007)* (pp. 475–475).
- 445 Fernández-Martínez, J. L., Fernández-Muñiz, Z., Pallero, J., & Pedruelo-González, L. M.
446 (2013). From bayes to tarantola: New insights to understand uncertainty in inverse
447 problems. *Journal of Applied Geophysics*, 98, 62–72.
- 448 Florio, G. (2020). The estimation of depth to basement under sedimentary basins from
449 gravity data: Review of approaches and the itresc method, with an application to the
450 yucca flat basin (nevada). *Surveys in Geophysics*, 41(5), 935–961.
- 451 Güntner, A., Schmidt, R., & Döll, P. (2007). Supporting large-scale hydrogeological mon-
452 itoring and modelling by time-variable gravity data. *Hydrogeology Journal*, 15(1),
453 167–170.
- 454 Jaffal, M., El Goumi, N., Kchikach, A., Aïfa, T., Khattach, D., & Manar, A. (2010). Gravity
455 and magnetic investigations in the haouz basin, morocco. interpretation and mining
456 implications. *Journal of African Earth Sciences*, 58(2), 331–340.
- 457 Li, W., Liu, Y., Li, B., & Luo, F. (2016). Hydrocarbon exploration in the south yellow sea
458 based on airborne gravity, china. *Journal of Earth Science*, 27(4), 686–698.
- 459 Li, Y., & Oldenburg, D. W. (1996). 3-d inversion of magnetic data. *Geophysics*, 61(2),
460 394–408.
- 461 Marini, F., & Walczak, B. (2015). Particle swarm optimization (pso). a tutorial. *Chemo-
462 metrics and Intelligent Laboratory Systems*, 149, 153–165.
- 463 Mishra, D., Gupta, S., & Venkatarayudu, M. (1989). Godavari rift and its extension towards
464 the east coast of india. *Earth and Planetary Science Letters*, 94(3-4), 344–352.
- 465 Montesinos, F., Arnos, J., & Vieira, R. (2005). Using a genetic algorithm for 3-d inversion of
466 gravity data in fuerteventura (canary islands). *International Journal of Earth Sciences*,
467 94(2), 301–316.
- 468 Nagihara, S., & Hall, S. A. (2001). Three-dimensional gravity inversion using simulated an-
469 nealing: Constraints on the diapiric roots of allochthonous salt structures. *Geophysics*,
470 66(5), 1438–1449.
- 471 Pallero, J., Fernandez-Martinez, J. L., Bonvalot, S., & Fudym, O. (2015). Gravity inversion
472 and uncertainty assessment of basement relief via particle swarm optimization. *Journal
473 of Applied Geophysics*, 116, 180–191.
- 474 Perez, R. l., & Behdian, K. (2007). Particle swarm approach for structural design opti-
475 mization. *Computers & Structures*, 85(19-20), 1579–1588.

- 476 Portniaguine, O., & Zhdanov, M. S. (2002). 3-d magnetic inversion with data compression
477 and image focusing. *Geophysics*, 67(5), 1532–1541.
- 478 Qin, P., Huang, D., Yuan, Y., Geng, M., & Liu, J. (2016). Integrated gravity and gravity
479 gradient 3d inversion using the non-linear conjugate gradient. *Journal of Applied*
480 *Geophysics*, 126, 52–73.
- 481 Qureshy, M., Brahmam, N. K., Garde, S., & Mathur, B. (1968). Gravity anomalies and the
482 godavari rift, india. *Geological Society of America Bulletin*, 79(9), 1221–1230.
- 483 Ramanamurthy, B., & Parthasarathy, E. (1988). On the evolution of the godavari gondwana
484 graben, based on landsat imagery interpretation. *Journal of Geological Society of India*
485 (Online archive from Vol 1 to Vol 78), 32(5), 417–425.
- 486 Rose, M., Zeng, Y., & Dransfield, M. (2006). Applying falcon® gravity gradiometry to
487 hydrocarbon exploration in the gippsland basin, victoria. *Exploration Geophysics*,
488 37(2), 180–190.
- 489 Roy, A., Dubey, C. P., & Prasad, M. (2021a). Gravity inversion for heterogeneous sed-
490 imentary basin with b-spline polynomial approximation using differential evolution
491 algorithm. *Geophysics*, 86(3), F35–F47.
- 492 Roy, A., Dubey, C. P., & Prasad, M. (2021b). Gravity inversion of basement relief using
493 particle swarm optimization by automated parameter selection of fourier coefficients.
494 *Computers & Geosciences*, 156, 104875.
- 495 Roy, A., & Kumar, T. S. (2021). Gravity inversion of 2d fault having variable density
496 contrast using particle swarm optimization. *Geophysical Prospecting*, 69(6), 1358–
497 1374.
- 498 Roy, L., Agarwal, B., & Shaw, R. (2000). A new concept in euler deconvolution of isolated
499 gravity anomalies. *Geophysical prospecting*, 48(3), 559–576.
- 500 Shelton, J. W. (1984). Listric normal faults: an illustrated summary. *AAPG Bulletin*,
501 68(7), 801–815.
- 502 Sheth, H. (1998). A reappraisal of the coastal panel flexure, deccan traps, as a listric-fault-
503 controlled reverse drag structure. *Tectonophysics*, 294(1-2), 143–149.
- 504 Shi, Y., & Eberhart, R. (1998). A modified particle swarm optimizer. In 1998 ieee inter-
505 national conference on evolutionary computation proceedings. *ieee world congress on*
506 *computational intelligence (cat. no. 98th8360)* (pp. 69–73).
- 507 Silva, J., Costa, D. C., & Barbosa, V. C. (2006). Gravity inversion of basement relief and
508 estimation of density contrast variation with depth. *Geophysics*, 71(5), J51–J58.
- 509 Silva, J., Santos, D., & Gomes, K. (2014). Fast basement relief inversion. *Geophysics*, 79(5),
510 G79–G91.
- 511 Song, M., Yi, P., Xu, J., Cui, S., Shen, K., Jiang, H., ... Wang, H. (2012). A step
512 metallogenetic model for gold deposits in the northwestern shandong peninsula, china.
513 *Science China Earth Sciences*, 55(6), 940–948.
- 514 Srivastava, S., Datta, D., Agarwal, B., & Mehta, S. (2014). Applications of ant colony
515 optimization in determination of source parameters from total gradient of potential
516 fields. *Near Surface Geophysics*, 12(3), 373–390.
- 517 Suess, E. (1909). *The face of the earth: Das antlitz der erde* (Vol. 4). Clarendon Press.
- 518 Talwani, M., Worzel, J. L., & Landisman, M. (1959). Rapid gravity computations for
519 two-dimensional bodies with application to the mendocino submarine fracture zone.
520 *Journal of geophysical research*, 64(1), 49–59.
- 521 Tinto, K., & Bell, R. E. (2011). Progressive unpinning of thwaites glacier from newly
522 identified offshore ridge: Constraints from aerogravity. *Geophysical Research Letters*,
523 38(20).
- 524 Toushmalani, R. (2013). Gravity inversion of a fault by particle swarm optimization (pso).
525 *SpringerPlus*, 2(1), 1–7.
- 526 Veiga, M. M., & Gunson, A. J. (2020). Gravity concentration in artisanal gold mining.
527 *Minerals*, 10(11), 1026.
- 528 Wan, L., & Zhang, J. (2019). Analytical solutions of gravity vector and gravity gradient
529 tensor caused by a 2d polygonal body with a 2d polynomial density contrast. *Surveys*
530 *in Geophysics*, 1–33.

- 531 Winckel, G. V. (2004). Legendre-gauss quadrature weights and nodes. MATLAB Cen-
532 tral File Exchange, ([https://www.mathworks.com/matlabcentral/fileexchange/4540-](https://www.mathworks.com/matlabcentral/fileexchange/4540-legendre-gauss-quadrature-weights-and-nodes)
533 [legendre-gauss-quadrature-weights-and-nodes](https://www.mathworks.com/matlabcentral/fileexchange/4540-legendre-gauss-quadrature-weights-and-nodes)).
- 534 Xin, J., Chen, G., & Hai, Y. (2009). A particle swarm optimizer with multi-stage linearly-
535 decreasing inertia weight. In 2009 international joint conference on computational
536 sciences and optimization (Vol. 1, pp. 505–508).
- 537 Yamada, Y., & McClay, K. (2003). Application of geometric models to inverted listric fault
538 systems in sandbox experiments. paper 1: 2d hanging wall deformation and section
539 restoration. *Journal of structural geology*, 25(9), 1551–1560.
- 540 Zhang, J., Wang, C.-Y., Shi, Y., Cai, Y., Chi, W.-C., Dreger, D., . . . Yuan, Y.-H. (2004).
541 Three-dimensional crustal structure in central taiwan from gravity inversion with a
542 parallel genetic algorithm. *Geophysics*, 69(4), 917–924.
- 543 Zhou, X. (2008). 2d vector gravity potential and line integrals for the gravity anomaly caused
544 by a 2d mass of depth-dependent density contrast. *Geophysics*, 73(6), I43–I50.
- 545 Zhou, X. (2009). General line integrals for gravity anomalies of irregular 2d masses with
546 horizontally and vertically dependent density contrast. *Geophysics*, 74(2), I1–I7.
- 547 Zhou, X. (2013). Gravity inversion of 2d bedrock topography for heterogeneous sedimentary
548 basins based on line integral and maximum difference reduction methods. *Geophysical*
549 *Prospecting*, 61(1), 220–234.